Observation of Exceptional Stability in a Nonlinear Optical Crystal Under Extreme Conditions

Yuejian Wang,* Victor T Barone, Sanjay V. Khare, Ankun Yang, Dongzhou Zhang, Young Jay Ryu, Sidharth Menon, Wei-lin Zhou, Prathisha Sri Kanthan, and Matthew Kozel

As a unique nonlinear optical material, $Ba_3(ZnB_5O_{10})PO_4$ (BZBP) boasts a range of distinctive properties, including low anisotropic thermal expansivity, high specific heat, minimal walk-off effect, large acceptance angle, non-hygroscopicity, and high conversion efficiency. These features position BZBP as a highly promising candidate for crucial components in ultraviolet (UV) laser systems. Notably, all previous studies have been conducted under ambient pressures. In this research, synchrotron X-ray diffraction and Raman spectroscopy are employed to investigate BZBP's behavior under extreme conditions. The findings revealed that BZBP remains exceptionally stable up to 43 Gigapascals (GPa), significantly extending its application range from ambient to high-pressure environments. This stability enhancement opens new avenues for utilizing BZBP in optical systems designed to function under extreme conditions. Additionally, the study determined BZBP's bulk modulus (110 GPa) and linear compressibility along each lattice axis. Theoretical computations are used to assign the Raman modes, characterize their corresponding lattice vibrations, validate the experimental results, and elucidate the mechanisms underlying the material's remarkable stability.

1. Introduction

The wavelength of a laser beam is crucial, in determining both its color and the energy it delivers. For example, green lasers

Y. Wang, S. Menon, W.-lin Zhou, P. S. Kanthan, M. Kozel
Physics Department
Oakland University
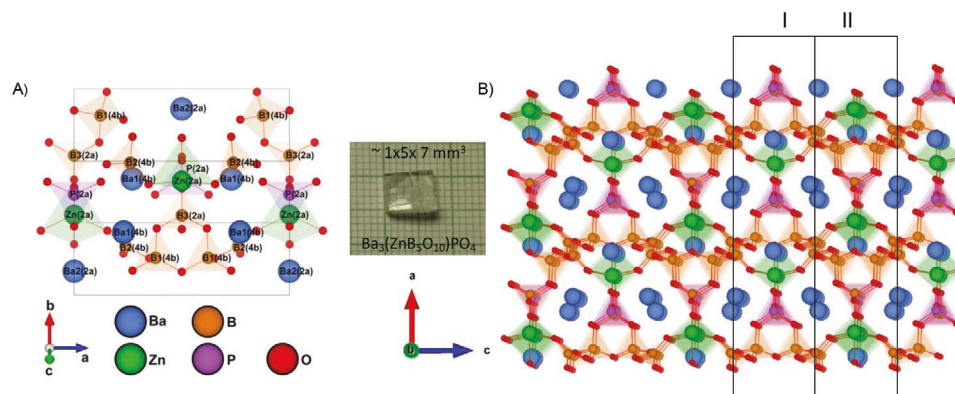Rochester, MI 48309, USA
E-mail: ywang235@oakland.edu

V. T Barone, S. V. Khare
Department of Physics and Astronomy, and Wright Center for Photovoltaics Innovation and Commercialization (PVIC)
The University of Toledo
Toledo, Ohio 43606, USA

A. Yang
Department of Mechanical Engineering
Oakland University
Rochester, MI 48309, USA

D. Zhang, Y. J. Ryu
Center for Advanced Radiation Sources
The University of Chicago
Chicago, IL 60637, USA

typically emit light between 520 and 532 nm, while red lasers range from 630 to 670 nm. Beyond color, wavelength plays a key role in laser performance, influencing its suitability for different applications. CO_2 lasers, commonly used in cutting and machining, operate at 10600 nm, while lasers for hair removal typically span from 600 to 1100 nm. With advancing technology, there is growing interest in pushing lasers into the deep-ultraviolet (DUV) spectrum, below 200 nm, to extend their use beyond visible light.

Unlocking the potential of DUV lasers presents significant challenges, requiring advanced nonlinear optical (NLO) materials that are essential for controlling laser characteristics, such as extending the radiation spectrum from UV to infrared (IR). Currently, $KBe_2BO_3F_2$ (KBBF) is the primary NLO material capable of generating DUV lasers. However, its production involves the hazardous BeO powder, making the process both cumbersome and costly.[1]

A promising breakthrough emerged with the development of $Ba_3(ZnB_5O_{1n})(PO_4)$ (BZBP), a unique NLO crystal.[2] Notably, BZBP avoids the challenges posed by KBBF, as it does not contain the hazardous element beryllium (Be). The synthesis of BZBP single crystals involved a precise two-step process: first, BZBP powders were produced by annealing carefully prepared mixtures of $BaCO_3$, ZnO, H_3BO_3, and $NH_4H_2PO_4$. These powders were then used to grow BZBP single crystals using a top-seed solution growth method, with additional H_3BO_3 and ZnO.[2,3]

The development of this crystal for DUV lasers has followed an inconsistent and complex path. Initially, detailed characterizations of the freshly grown BZBP single crystals revealed promising attributes.[2,3] Notably, DUV absorption tests demonstrated BZBP's transparency to radiation in the DUV spectrum, positioning it as a potential NLO material for DUV lasers. However, recent studies have shown that BZBP cannot achieve phase matching in the DUV region, suggesting that it is unsuitable for generating DUV lasers despite its early promise.[4]

Nevertheless, this inconsistency does not undermine the significance of BZBP. A more thorough investigation into related compounds is necessary to fully emphasize BZBP's distinctive advantages. BZBP shares many characteristics with borate- and phosphate-based NLO materials, such as BBO (Beta-Barium Borate) and LBO (Lithium Triborate), both recognized for their

**ADVANCED
SCIENCE NEWS**

www.advancedsciencenews.com

**ADVANCED
FUNCTIONAL
MATERIALS**

www.afm-journal.de

Figure 1. A) Crystal structure of BZBP within a unit cell. Ba polyhedra, Ba bonds, and the labels of O atoms are omitted for clarity. Atomic indices are not shown for Zn and P, as there is only one unique position for each element. B) Visualization of the crystal structure observed along the *b*-axis at ambient conditions. The inset between (A,B) is an optical image of the BZBP crystal.

strong NLO responses, high laser damage thresholds, and broad transparency ranges.[5] For instance, BBO features a transparency range from 189 nm to 3.5 μm and is frequently used in high-power laser systems, particularly for UV and visible light generation, while LBO offers phase-matching capabilities from 160 nm to 2.6 μm. Other materials, like KTP (Potassium Titanyl Phosphate), are known for their high NLO efficiency in the visible and infrared regions.[5b] In comparison, BZBP distinguishes itself through its high optical and thermal stability, low anisotropic thermal expansivities, large specific heat, high thermal conductivity, small walk-off effect, large acceptance angle, non-hygroscopicity, and high conversion efficiency—making it a strong candidate for UV photonic applications.[2–4]

Previous assessments of BZBP were conducted solely at room or high temperatures under ambient pressure conditions. However, pressure is a critical factor influencing a material's state, properties, and applications. For instance, carbon can exist as either soft graphite or super-hard H-carbon depending on the pressure.[6] Therefore, studying materials under high-pressure is essential for understanding fundamental properties such as deformation, stability, and phase transitions, as well as exploring the mechanisms behind pressure-induced changes.

From a practical perspective, understanding high-pressure behavior is crucial for a material's application, especially under high-pressure conditions. A material must demonstrate high stability to be suitable for tasks in such environments. Recognizing this, we conducted high-pressure measurements of BZBP using a diamond anvil cell, synchrotron X-ray diffraction, and Raman spectroscopy. Our results revealed that BZBP maintains its structural stability under compression up to pressures exceeding 40 GPa and heating up to 850 K, without undergoing any phase transitions. The experimental findings were supported by theoretical computations, which extensively explored the mechanisms governing structural stability.

The exceptional structural stability and relatively low anisotropic linear compressibility suggest that BZBP may retain its distinctive optical properties even under high-pressure conditions. This opens new possibilities for applying NLO materials in extreme or harsh environments. Notably, while 43 GPa exceeds the typical range for many optical materials, it offers a substantial margin for practical applications. The
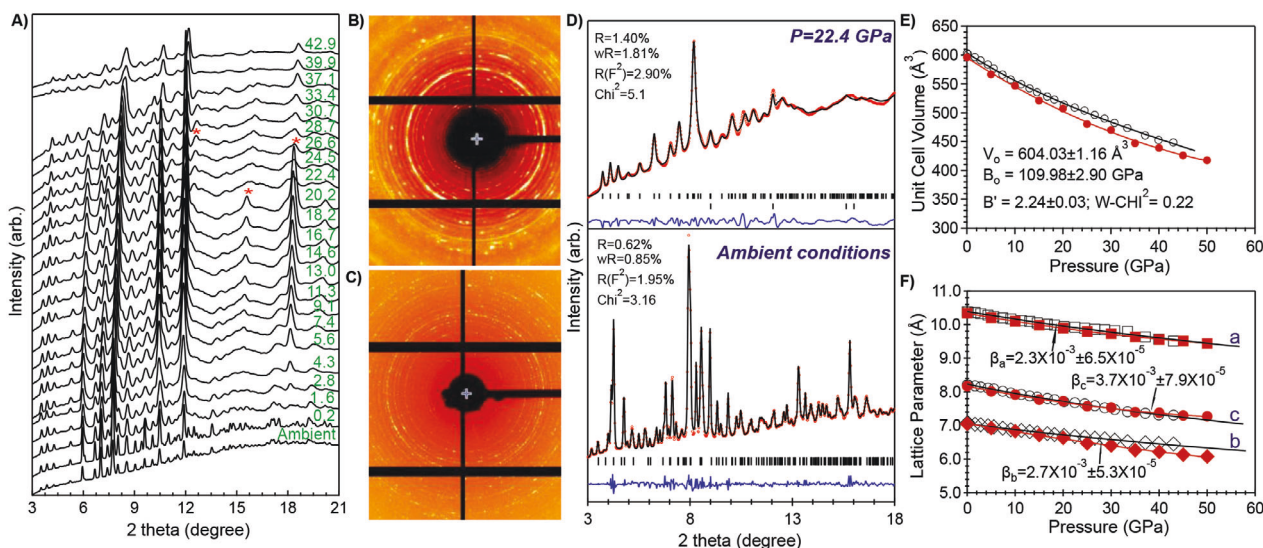
material's ability to withstand such pressures without structural failure provides valuable insights into its performance limits and ensures functionality and reliability under more moderate high-pressure conditions.

2. Results and Discussion

2.1. Ultra-Stability in BZBP Detected by High-Pressure Synchrotron X-Ray Diffraction

This study commenced with a single-crystal of BZBP, synthesized using a top-seed solution growth method.[2,3] While detailed crystal structure information for BZBP is available elsewhere,[2] here we provide a brief overview. At ambient conditions, BZBP crystallizes in an orthorhombic structure, as shown in **Figure 1**. The unit cell of BZBP contains two unique Ba atoms: one at Wyckoff position 4b and the other at 2a. There are also three unique B atoms, with two located at position 4b and one at 2a. Additionally, there is one unique Zn atom and one unique P atom, both situated at Wyckoff position 2a. The structure includes nine O atoms, with five at position 4b and four at position 2a. Ba, Zn, B, and P atoms are positioned at the centers of polyhedra, with the O atoms at the vertices, as illustrated in Figure 1A. Figure 1B shows that the chain structures of I and II form the crystal structure of BZBP.

The single-crystal was then crushed into fine powders for X-ray diffraction measurements. We thoroughly examined the powdered BZBP by collecting synchrotron X-ray diffraction data at ambient conditions. The X-ray pattern confirmed that the sample was pure BZBP, with no detectable impurities. As shown in Figure 2, the X-ray diffraction pattern closely matched the noncentrosymmetric orthorhombic structure of the $Pmn2_1$ space group (#31), with lattice parameters of 10.38415, 7.07683, and 8.21287 Å. These results are consistent with previous studies.[2] Following the collection of the ambient X-ray pattern, the sample was compressed, and X-ray patterns were recorded at various pressure points. As illustrated in **Figure 2A**, the Bragg reflections gradually shifted to higher angles with increasing pressure, reflecting the reduction in spacing between atomic layers under compression. Notably, up to ≈43 GPa, no phase transition was

**ADVANCED
SCIENCE NEWS**

www.advancedsciencenews.com

**ADVANCED
FUNCTIONAL
MATERIALS**

www.afm-journal.de

Figure 2. A) X-ray diffraction patterns of the sample at various pressure points. Red stars indicate peaks from the rhenium (Re) gasket. Green numbers represent the pressures in GPa at which the patterns were collected. B,C) Raw X-ray profile rings of the sample collected at ambient conditions and 22.4 GPa, respectively. D) Examples of Rietveld refinements of the X-ray diffraction patterns. The collected patterns are shown as red open circles, while the calculated patterns are depicted by solid black curves. The blue curve at the bottom represents the difference between the collected and calculated patterns. Vertical bars above the blue curve indicate the peak positions of the diffraction profile for each pressure point. At 22.4 GPa, X-ray diffraction captured signals from both the sample and gasket materials, resulting in four vertical bars for Re signals. The representative refinement results, including lattice parameters and atomic positions along with their associated uncertainties, are provided in Table S1 (Supporting Information). E) Unit cell volumes (black open circles) fitted using the third-order Birch–Murnaghan equation of state, with the fitting result shown by the black solid curve. Red dots and lines represent theoretical computations. F) Lattice parameters a, b, and c (open black symbols) versus pressure, with fitting curve from Equation (2) shown as black lines. The red ones represent theoretical computations.

observed, demonstrating the thermodynamic stability of the crystal structure under high-pressure conditions.

The abrupt change in X-ray diffraction pattern quality from 0.2 to 1.6 GPa is attributed to the brittleness of the BZBP material. Under these pressure conditions, the material tends to break or crush into very fine powders, leading to peak broadening in the X-ray diffraction patterns. We continuously monitored the hydrostatic conditions using fluorescence measurements from three rubies placed in the sample chamber, which confirmed that the pressure-transmitting medium's hydrosticity was well-maintained at these pressures. However, as pressure increased, the reduction in grain size and even partial amorphization of the material, along with the loss of hydrostatic conditions, contributed to localized concentrations of deviatoric stress within the sample. Consequently, with increasing pressure, the Bragg reflections became broader, less intense, and even asymmetric, as shown in Figures 2B,C.

The lattice parameters and unit cell volumes at each pressure point were obtained through the Rietveld refinement of the X-ray patterns using GSAS-II.[7] Examples of the refined diffraction profiles are shown in Figure 2D. The dataset of unit cell volume versus pressure was then fitted to a third-order Birch–Murnaghan equation of state,[8]

$$P(V) = \frac{3B_o}{2}\left[\left(\frac{V_o}{V}\right)^{\frac{7}{3}} - \left(\frac{V_o}{V}\right)^{\frac{5}{3}}\right]\left\{1 + \frac{3}{4}\left(B_o' - 4\right)\left[\left(\frac{V_o}{V}\right)^{\frac{2}{3}} - 1\right]\right\} \quad (1)$$

where B_o is the bulk modulus, B_o' stands for the derivative of the bulk modulus with respect to pressure, V_o represents the unit cell volume at ambient conditions, and V refers to the volume at a given pressure point, as shown in Figure 2E. The software of EosFit7GUI [9] was employed for the least-square fitting, yielding $B_o = 109.98 \pm 2.90$ GPa, $B_o' = 2.24 \pm 0.03$, and $V_o = 604.03 \pm 1.16$ Å^3. Considering the uncertainty, the value of 604.03 $\pm$ 1.16 Å^3 aligns closely with the value of 602.6(11) Å^3 determined in the previous study.[2] It's crucial to note that these uncertainties stem from the fitting process, and the propagation of uncertainties from pressure and volume values was not included. The computational results are slightly smaller than the experimental measurements, but overall, they are in good agreement, as shown in Figure 2E.

In addition to examining phase transitions and the equation of state, our investigation extends to the linear compressibility of the sample along each of the lattice axes (a, b, and c), as shown in Figure 2F. To determine the compressibility for each lattice direction, we employed a pseudo-Birch–Murnaghan equation of state, as formulated in Equation (2). In this approach, the unit cell volumes are substituted with the lattice parameters, and B_o' is set to 4.

$$P(l) = \frac{3}{2\beta}\left[\left(\frac{l_o}{l}\right)^{\frac{7}{3}} - \left(\frac{l_o}{l}\right)^{\frac{5}{3}}\right] \quad (2)$$

where P the sample pressure; β: the linear compressibility along individual lattice axis; l_0: the lattice parameter at ambient

pressure and room-temperature; l: the lattice parameter at a given pressure point.

Typically, linear compressibility is positive for most materials, as the lattice shortens under compression. However, some rare materials exhibit negative compressibility along one or more lattice directions, meaning these lattices elongate under high-pressure rather than shortening as is common.[10,7] For the present material, while all lattice parameters decrease with pressure, as shown in Figure 2F, the relatively small compressibility values indicate that the lattices are quite stiff. Moreover, the changes in lattice parameters with pressure are not uniform. Over the studied pressure range, lattice parameter "a" experiences the least shortening, demonstrating the lowest compressibility. This variation is due to the non-homogeneous distribution of atoms in the crystal structure. As depicted in Figure 1, the alternating Ba—O and P—B—O atomic layers are aligned along lattice "a," creating a densely packed arrangement that limits the significant reduction in atom spacing and results in lower compressibility. In contrast, the larger gaps between atoms and lower atomic density along lattices "b" and "c" permit greater flexibility and freer movement of atoms in these directions, leading to higher linear compressibility. A small difference, consistent with expected experimental error, is also observed between the experimental and computational results. As shown in Figure 2F, the experimental and computational values for lattice parameter "a" are nearly identical, whereas the computed values for lattice parameter "c" are slightly larger than the measured ones, and the opposite is true for lattice parameter "b."

2.2. Ultra-Stability in BZBP Confirmed by High-Pressure/High-Temperature Raman Spectroscopy

Although BZBP is an extraordinary optical material, its Raman features have not been comprehensively studied until the present research. In this study, density functional theory (DFT) was utilized to perform band component analysis and to assign the active Raman modes. According to the symmetry information for space groups, BZBP belongs to the C_{2v} point group. It consists of one Ba, one Zn, one B, one P, and four O atoms at the 2a Wyckoff positions, and one Ba, two B, and five O atoms at the 4b positions. Each 2a position features two A_1, one A_2, one B_1, and two B_2 vibrational modes, while the 4b positions exhibit three of each A_1, A_2, B_1, and B_2 modes.[11] This crystal includes numerous active Raman modes, which are detailed in Table SII (Supporting Information).

Figure 3 illustrates the assignment of Raman-active modes to DFT vibrational frequencies. Figure 3A presents the experimentally measured Raman activity of BZBP, including the band indices of modes that can be matched to modes computed with DFT. Insets in Figure 3A highlight the atomic vibrations responsible for the modes with the most prominent intensities. The indices correspond to the bands shown in Figure 3B at the Γ point. Only atomic vibrations with amplitudes exceeding 0.1 Å are depicted, and we provide commentary solely on those atoms.

Raman-active modes below 230 cm^{-1} are present, but the high density of states in this region, as shown in Figure 3C, makes band assignment challenging. According to the DOS, all elements in BZBP contribute to these modes, with Ba and O vibra-

tions being particularly significant. Above 230 cm^{-1}, Ba's contribution diminishes, and many high-intensity peaks observed in Figure 3A are attributed to vibrations of B and O atoms. Zn contributes weakly up to ≈600 cm^{-1} before going to zero contribution. Meanwhile, P mode are active in specific wavenumber ranges, notably ≈550 and 1000 cm^{-1}.

The dynamical stability of BZBP under pressure is confirmed by the absence of imaginary phonon modes across the entire simulated pressure range, from 0 to 50 GPa. Although the phonon band structure in Figure 3B shows at least one band with an imaginary (negative) frequency, further investigation reveals that these bands correspond to purely translational modes, which are not relevant for assessing material stability. Translational modes are indicated as dotted curves in Figure 3B.
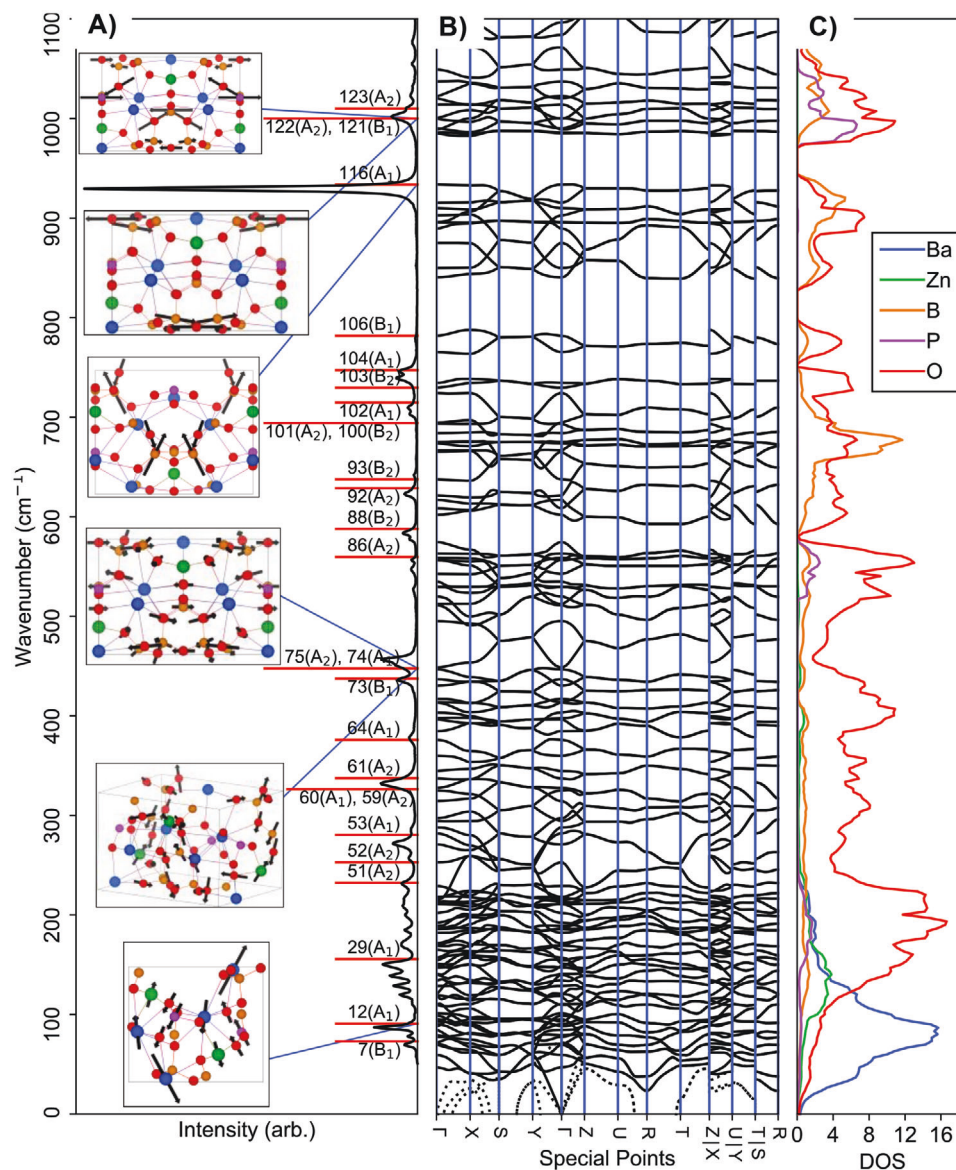
The peak at 87 cm^{-1} is associated with mode 12 (A_1). This mode's vibrations primarily occur in the a,b plane, with Ba atoms at position 4b exhibiting vibrations in the a–c plane. Mode 12 involves contributions from all Ba, P, and Zn atoms, with only a few O atoms participating. The O atom oscillations are aligned with those of the P atoms and are approximately antiparallel to the movements of Ba and Zn.

The Raman peak at 457 cm^{-1} originates from modes 74 (A_1) and 75 (A_2). Mode 74 features vibrations of the Zn and B atoms at positions 2a within the a–c plane, accompanied by O atoms moving in multiple directions. Mode 75 demonstrates a "shearing" effect on the central O_3B_3 hexagonal structure along the c direction. Some O atoms at positions 4b contribute significantly to this mode, though their vibration directions are inconsistent. B atoms involved in this mode move exclusively within the a–c plane.

The mode with the highest measured intensity, at 930 cm^{-1}, is assigned to band 116 (A_1). This mode is primarily due to an O atom at position 4b vibrating in the b,c plane, along with a B atom at position 4b, also vibrating in the b,c plane. All vibrations are approximately two-thirds aligned with the b lattice vector and one-third with the c vector. The motion of O and B along b is out-of-phase, while their vibrations along c are in-phase.

Finally, the degenerate modes indexed as 121 (B_1) and 122 (A_2) are responsible for the Raman peak at 1002 cm^{-1}. Mode 121's predominant vibrations occur along the c lattice vector, involving a B atom at Wyckoff site 4b moving opposite to two of the four O atoms it is bonded to—one at site 2a and the other at site 4b. The O atom at 2a vibrates with approximately four times more intense than the O atom at 4b. Mode 122 involves P in addition to O and B. The P atom at 2a vibrates along the c lattice vector, as does a B atom at position 4b and an O atom at 2a to which it is bonded. An O atom at position 4b, bonded to the aforementioned P atom, moves in the a–c plane.

At room-temperature, we conducted high-pressure measurements on a single-crystal of BZBP, as shown in **Figure 4A,B**. Compared to the Raman spectrum obtained from the bulk sample under normal conditions, the high-pressure Raman spectra exhibit a faint signal with only one discernible active mode, mode 116, amidst the background diffusion scattering. The reduced signal strength is attributed to the limited size of the sample compressed within the sample chamber (≈100 μm in diameter), as well as interference from the diamond anvils causing blockage, scattering, and absorption. Consequently, our analysis focuses

**ADVANCED
SCIENCE NEWS**

www.advancedsciencenews.com

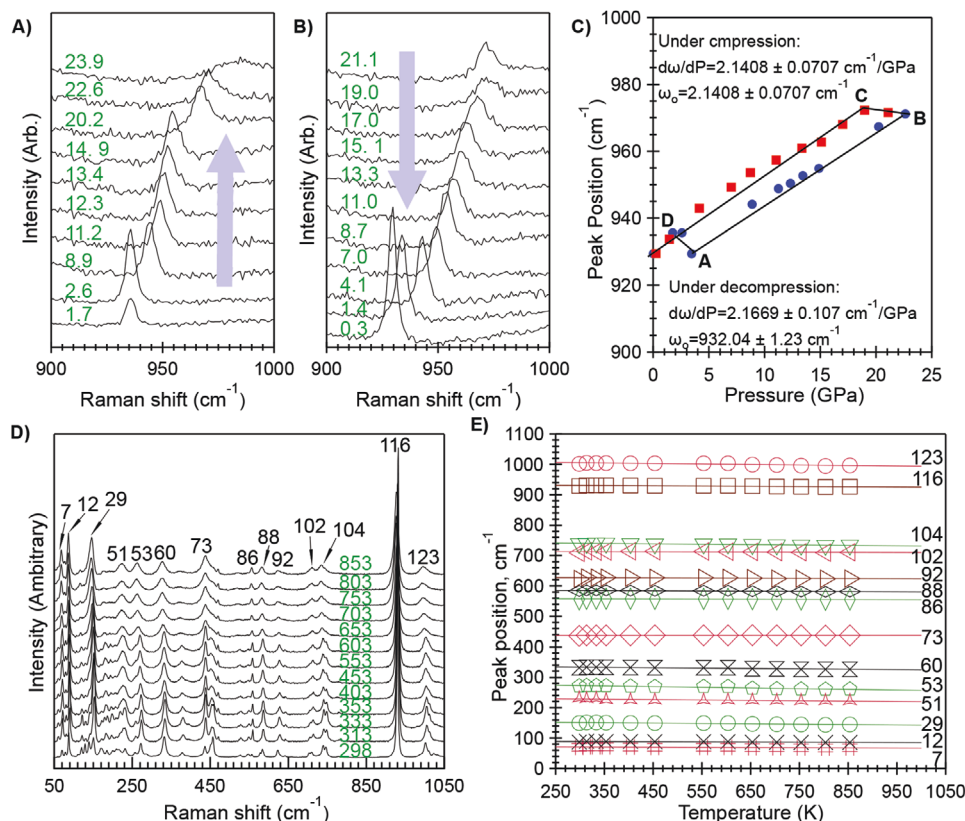**ADVANCED
FUNCTIONAL
MATERIALS**

www.afm-journal.de

Figure 3. A) Measured Raman spectra of BZBP. Raman-active peaks are marked with red lines and indexed with their corresponding modes in parentheses. Insets show the atomic movements responsible for the Raman-active modes discussed in the Results – Vibrational Modes section. B) DFT-computed phonon band structure of BZBP. C) DFT-computed phonon density of states (DOS) for BZBP, with DOS values expressed in units of 10^2 states cm atom^{-1}.

on this Raman mode to characterize the optical properties of the material.

During compression, Raman mode 116 gradually shifted to higher wavenumbers, as depicted in Figure 4A. At 23.9 GPa, this Raman peak became a broad and low-intensity bump, suggesting that further increases in pressure might be detrimental. This reduction in Raman feature could be due to the thinning and potential collapse of the sample under high-pressure along the axial direction. Additionally, an electrical phase transition, such as a transformation from an insulator or semiconductor to a conductor, might be occurring, though this is beyond the scope of the current study. Upon decompression, the peak intensity increased as pressure was released, as shown in Figure 4B. A clear

hysteresis was observed between the peak position and pressure throughout the entire compression and decompression cycle, as depicted in Figure 4C. Compression-induced stress altered the bond lengths, angles, and coordination environments around the Raman-active modes, thereby affecting their frequencies. The kinetics of structural condensation and relaxation during compression and decompression may contribute to the observed hysteresis in the Raman peak position. Importantly, no crystal structural phase transformation was detected during these high-pressure Raman measurements.

We calculated the pressure coefficients, $\frac{d\omega}{dP}$, by fitting the Raman peak positions against pressures. Due to hysteresis during compression and decompression, data from segments AB

**ADVANCED
SCIENCE NEWS**

www.advancedsciencenews.com

**ADVANCED
FUNCTIONAL
MATERIALS**

www.afm-journal.de

Figure 4. Raman spectra collected under various conditions: A) During compression; B) During decompression; C) Relationship between peak position and pressure throughout the compression-decompression cycle; D) During heating; E) Peak position versus temperature, with solid lines representing the linear fitting results. Green numbers in A,B) indicate the pressures in GPa during the compression and decompression processes. Green numbers in D) denote the temperatures in Kelvin during heating. Black numbers in D,E) correspond to the indices of the Raman bands.

(compression) and CD (decompression) were utilized to determine the pressure coefficients, as demonstrated in Figure 4C. The two sets of values are closely aligned, as evidenced by the nearly parallel fitting lines for AB and CD. Additionally, Grüneisen parameters (γ) were computed using the formula $\gamma = \frac{B_o}{\omega_o}\left(\frac{d\omega}{dP}\right)$, where ω_o represents the peak positions of the Raman modes under ambient conditions, $\frac{d\omega}{dP}$ denotes the pressure coefficient, and B_o is the bulk modulus obtained from fitting volume-pressure data. Interestingly, the calculation yielded the same values, $\gamma = 0.25 \pm 0.01$, for both compression and decompression. The value of the Grüneisen parameter is crucial for further understanding the thermodynamic, mechanical, and structural properties of this material.

In addition to high-pressure study, we also conducted the high-temperature Raman investigation on this material. As shown in Figure 4D, the Raman spectra reveal a gradual shift of the active Raman modes toward lower wavenumbers with increasing temperature, indicative of a redshift.

The Raman shift positions versus temperatures for all of the resolvable Raman modes are illustrated in Figure 4E, exhibiting a negative trend by a linear fitting,

$$\omega_t = \omega_o + \left(\frac{\partial \omega_t}{\partial T}\right)_P \Delta T \tag{3}$$
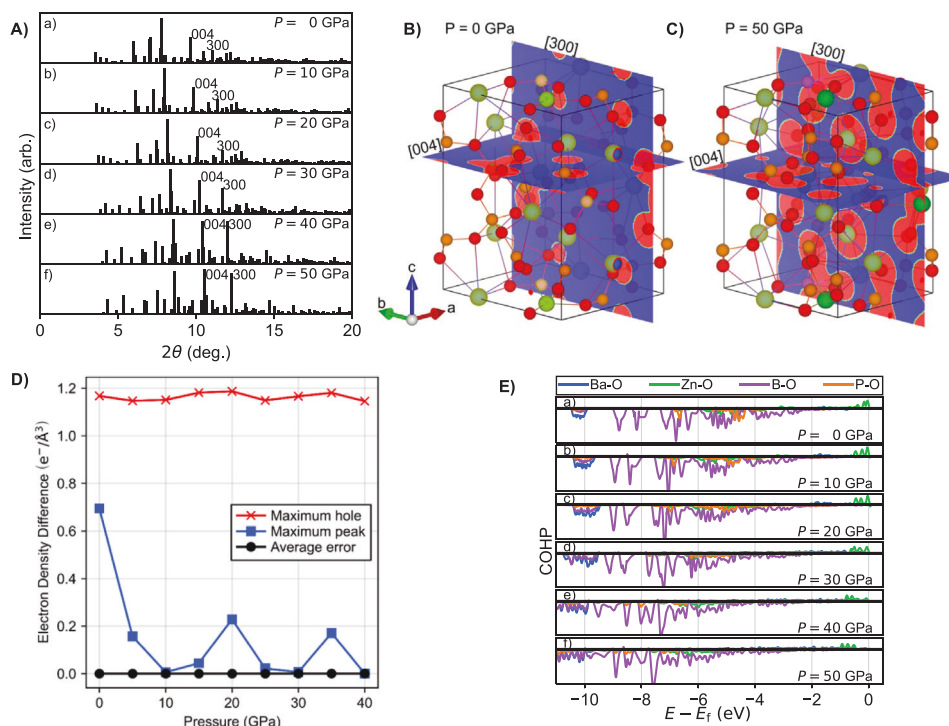
where $\omega_t, \omega_o, and\ \frac{\partial \omega_t}{\partial T}$, represent the Raman mode frequency at a given temperature, the Raman mode frequency at the temperature of 0 Kelvin (K), and the first-order temperature coefficient, respectively. All of those values obtained from the linear regression are listed in Table SIII (Supporting Information). There is no rise of a new vibrational band along with the very slow shift of the Raman modes during the heating, giving us evidence that this material remains stable even under high-temperature conditions.

2.3. Mechanism Behind the Ultra-Stability in BZBP

From a computational perspective, we sought to elucidate the mechanism behind the high stability of BZBP. Simulated powder X-ray diffraction patterns as a function of pressure are shown in **Figure 5A**. The X-ray diffraction profile displays a rightward shift in peak intensities with minimal alteration to the overall pattern, except for the notable [004] and [300] peaks, which are discussed later. This rightward shift is consistent with the contraction of lattice constants under pressure. The overall pattern's consistency suggests that the atomic structures remain similar throughout the entire pressure range.

The peaks with Miller indices [004] ($\approx 2\theta = 10°$) and [300] ($\approx 2\theta = 12°$) exhibit increased intensity with rising pressure. This

**ADVANCED
SCIENCE NEWS**

www.advancedsciencenews.com

**ADVANCED
FUNCTIONAL
MATERIALS**

www.afm-journal.de

Figure 5. A) Simulated X-ray diffraction patterns for the computational BZBP unit cell under various pressures, using X-ray light with a wavelength of 0.434 Å. B,C) Electronic density maps along the [004] and [300] Bragg planes for BZBP at 0 and 50 GPa, respectively. Electron densities are modeled as element-specific spheres centered at each atom, with a resolution of 0.05 Å. D) Differences between measured and predicted electron densities as a function of pressure, where holes represent less measured density than predicted and peaks represent more measured density than predicted. E) Crystal Orbital Hamilton Populations (COHP) for BZBP under pressure, with bonding contributions shown below and antibonding contributions above the horizontal black line.

phenomenon could typically suggest a phase transition; however, that is not the case here. Instead, the lattice parameters decrease non-uniformly with pressure, causing atoms that do not intersect certain Bragg planes at 0 GPa to intersect those planes at higher pressures. This behavior is illustrated in Figure 5B,C, which show model electron densities on the [004] and [300] planes at 0 and 50 GPa. The electron densities are modeled as spherical, a common approach for simulated powder X-ray diffraction patterns.[12] The VESTA visualization software was used to create these figures.[13]

In BZBP, the [300] plane at 0 GPa is near, but does not intersect, a few O and B atoms. At 50 GPa, however, the [300] plane intersects Ba and O atoms, significantly increasing the electron density on that plane. Although the overall structure of BZBP remains unchanged, this increase in electron density leads to a higher simulated diffraction intensity for the [300] peak under pressure. A similar effect occurs for the [004] plane, where the interaction with O and Ba atoms is less direct, leading to a more modest increase in peak intensity with pressure. This explains the observed enhancement in intensity for these peaks as pressure increases.

To ensure good correspondence between experimental measurements and theoretical calculations, we calculated the differences in electron density between the results of Rietveld refinement and theoretical models as a function of pressure, as shown in Figure 5D. The VESTA software was used to generate the den-

sity maps. At most, the theoretical models overestimate the measured electron density by 1.2 $e^-/Å^3$ and underestimate it by 0.7 $e^-/Å^3$. On average, the errors are consistently below 0.001 $e^-/Å^3$.

These discrepancies in the electron density maps are primarily attributed to barium atoms. The error, as a function of spatial coordinates, exhibits clear, localized maxima at the positions of the barium atoms. Given that barium is in the sixth row of the periodic table, while the other elements in BZBP are in the fourth, third, and second rows, such magnitude of error is expected due to its larger size. Additionally, our theoretical models do not account for finite-temperature effects.

Finally, symmetry analysis of the atomic structures indicates that BZBP retains the space group $Pmn2_1$ and point group C_{2v} across all simulated pressures. On average, the deviations in atomic positions between BZBP at 0 GPa and BZBP at 10, 20, 30, 40, and 50 GPa are 0.06, 0.15, 0.36, 0.52, and 0.55 Å, respectively. This increasing deviation is attributed to the non-uniform compression of the lattice vectors—see Figure 2F—rather than to any phase transitions. This is supported by the symmetry analysis and the discussion of the X-ray diffraction patterns presented earlier.

Figure 5E presents the results of the COHP for BZBP at various pressures. The COHP values reflect bonding contributions—the pair interactions responsible for material stability. Although the COHP values shown in Figure 5D are unscaled, their negative values clearly indicate that the material is exceptionally stable.[14]

**ADVANCED
SCIENCE NEWS**

www.advancedsciencenews.com

**ADVANCED
FUNCTIONAL
MATERIALS**

www.afm-journal.de

Overall, B—O bonds contribute ≈75% to the COHP, while P—O bonds contribute ≈15–20%. The remaining bonds, Ba—O and Zn—O, contribute ≈5% and 3%, respectively. With increasing pressure, B—O bonds show a slight increase in their contribution to the COHP, while P—O bonds exhibit a slight decrease—≈1–2% change between simulations at 0 and 50 GPa for both cases.

Additionally, we calculated the integrals of COHP up to the Fermi level, which provides insights into the strength of individual bonds. The integrals reveal that individual P—O bonds are the strongest, with B—O bonds being ≈60–75% as strong. Zn—O bonds exhibit ≈10% of the strength of P—O bonds, and Ba-O bonds are ≈5% as strong. Despite variations in pressure, the general order of bonding strengths (P—O > B—O > Zn—O > Ba—O) remains consistent, although B—O bonding strength shows a significant decrease. At 0 GPa, B—O bonds are 75% as strong as P—O bonds, but at pressures of 20 GPa and above, B—O bonds diminish to only 60% of the strength of P—O bonds. Ba—O and Zn—O bonds do not exhibit this behavior.

An anonymous reviewer noted the intriguing finding that, according to our COHP calculations, P—O bonds are stronger than B—O bonds. This result is unexpected under normal circumstances, where one might anticipate the opposite. Our findings can be attributed to the varying bonding environments of oxygen, boron, and phosphorus atoms in BZBP.

The number of bonding states available to an atom, and thus the bond strength, is influenced by its local environment. In BZBP, considering only the first nearest-neighbor interactions, oxygen can be coordinated by five distinct combinations of barium, zinc, phosphorus, and boron atoms. By distinguishing between oxygen atoms based on their local environments, the integrated COHP for each oxygen bond provides insight into the bonding strength relative to these environments.

The results of this analysis show that the integral of the COHP for P—O bonds is ≈−10 eV, regardless of the oxygen's local environment. In contrast, the values for B—O bonds range from −8.7 to −11.1 eV. Though this variation in chemical environments within the BZBP structure allows for B—O bonds that can be either stronger or weaker than P—O bonds, majority of B—O bonds are weaker than P—O bonds. Consequently, on average, BZBP exhibits weaker B—O bonds compared to P—O bonds.

The total integrated COHP values at the Fermi levels of BZBP under varying pressures, as listed in **Table 1**, are projected to increase with pressure while remaining negative between 0 and 50 GPa, indicating continued stability. This increase is mainly due to the weakening of B—O bonds, although this effect is partially offset by the relatively stable P—O bonds, which are expected to strengthen slightly by ≈3% from 0 to 50 GPa.

The formation energies of BZBP calculated at various pressures are summarized in Table 1. The formation energies are given with respect to the constituent elements Ba, Zn, B, P, and O. The formation energies are consistently negative, ranging from -72 eV/f.u. at 0 GPa to −61 eV/f.u. at 50 GPa. While the predicted formation energies increase with pressure, they remain negative throughout, demonstrating that BZBP maintains energetic stability across all tested pressure conditions.

Table 1. Calculated formation energies of BZBP at various pressures per formula unit (f.u.), and the total integrated COHP.

Pressure [GPa]	Formation energy [eV/f.u.]	Integrated COHP [eV/pair]
0	−72.4	−2.45
5	−72.1	−2.24
10	−71.6	−2.21
15	−70.6	−2.07
20	−69.9	−2.05
25	−68.2	−1.96
30	−67.3	−1.99
35	−65.2	−1.94
40	−64.3	−1.96
45	−62.6	−1.90
50	−61.3	−1.89

3. Conclusion

In summary, we conducted a thorough study of BZBP under extreme conditions. The X-ray diffraction analysis addressed various aspects, including lattice parameters, linear compressibility, and potential phase transitions, offering a comprehensive understanding of BZBP's behavior under pressure. Additionally, we examined BZBP's Raman features, providing detailed assignments of Raman-active modes through DFT calculations. Our findings underscore BZBP's stability, with minimal shifts in Raman modes under high-pressure and temperature. Theoretical computations further clarify the mechanisms behind the exceptional stability of this optical crystal, focusing on bond strength and formation energy.

Overall, this manuscript highlights both the ultra-stability of BZBP under high-pressure and high-temperature conditions and the underlying mechanisms responsible for its stability. This study is systematically detailed, providing valuable insights into BZBP's structural stability and unique optical properties under extreme conditions, and laying a solid foundation for future advancements in high-pressure optical applications.

4. Experimental Section

High-Pressure Experimental Method: To subject the material to high-pressure conditions, a diamond anvil cell with a pair of 300 μm culet-sized diamonds was utilized. The sample for high-pressure measurements comprised BZBP powders, which were obtained by crushing single crystals into fine particles. These powders were compressed within a sample chamber—a hole measuring 130 μm in diameter and ≈45 μm deep—created in a rhenium gasket using an electrical discharge machining system. Pressure applied to the samples was determined using Ruby fluorescence as a pressure gauge.[15] Ruby spheres were placed in the sample chamber, as close to the sample as possible, to ensure accurate pressure measurements. Ruby pressures were recorded both before and after acquiring X-ray data at each pressure point, and the average of these two readings was used as the sample pressure.

Before conducting high-pressure measurements, helium gas was introduced into the sample chamber of the diamond anvil cell as the pressure-transmitting medium (PTM). This ensured that the sampling materials, fully immersed in the PTM, experienced a minimal pressure gradient during measurements.[16] Helium gas injection into the sample chamber was

performed using a gas loading system at GSECARS of Argonne National Laboratory.[17]

High-pressure synchrotron powder X-ray diffraction patterns were obtained at beamline 13-BM-C of the Advanced Photon Source (APS) at Argonne National Laboratory. A membrane system automatically adjusted the sample pressure to enhance data collection efficiency. Incident monochromatic X-rays with a wavelength of 0.434 Å were focused to a size of 12 µm (horizontal) × 18 µm (vertical). X-ray diffraction patterns were recorded using a Pilatus 1 M area detector. Initially, an ambient diffraction pattern of powdered LaB$_6$ was collected to accurately determine the distance between the sample and the image plate, as well as the tilt of the image plate. The X-ray Debye ring collected at each pressure point was converted into conventional diffraction patterns using Dioptas.[18] Subsequently, GSAS-II was used to process the data, extracting molecular-level characteristics such as lattice parameters and atomic positions.[7] VESTA was employed for visualizing and illustrating the crystal structures of the sample.[13]

High-pressure Raman measurements were conducted using a Horiba Labram Raman spectrometer equipped with a green laser (532 nm wavelength) and a 600 g cm^{-1} grating. Temperature control during the heating process was provided by a Linkam Stage, which allows precise temperature adjustments ranging from −196 to 600 °C.

Density Functional Theory: The Vienna Ab Initio Simulation Package (VASP, version 6.1.0) was utilized for all DFT calculations.[19] Standard projector augmented wave (PAW) potentials were employed to represent the core electrons,[20] incorporating the following valence electrons: 5s^2 5p^6 6s^2 for barium, 3d^{10} 4p^2 for zinc, 2s^2 2p^1 for boron, 3s^2 3p^3 for phosphorus, and 2s^2 2p^4 for oxygen. Exchange-correlation effects were treated using the PBEsol functional.[21]

In VASP, a plane wave basis set was used, including all plane waves with energies below 450 eV.[22] Integrations were performed on a k-point grid with a uniform spacing of ≈3 Å^{-1}. Electron partial occupancies were handled using the tetrahedron method with Blöchl corrections.[23] At each pressure, atoms were relaxed until the force on each atom did not exceed 1 meV Å^{-1}.

The Phonopy code was used to compute the vibrational frequencies of BZBP employing a single conventional unit cell.[24] We ensured that the size of the simulation cell was large enough to converge the modes by using density functional perturbation theory (DFPT), implemented in VASP, to calculate the same frequencies. The maximum disparity in wavenumbers between finite differences and DFPT was 2.4 cm^{-1}, with an average difference of 0.2 cm^{-1}. Additionally, Phonopy was employed to compute the phonon band structure and DOS.

For COHP analysis, The local orbital basis suite toward electronic-structure reconstruction (LOBSTER, version 4.0.0) was used.[14,25] The plane wave basis was projected onto the following basis functions for barium, zinc, boron, phosphorus, and oxygen: 6s 5p$_y$ 5p$_z$ 5p$_x$ 4d$_{xy}$ 4d$_{yz}$ 4d$_z^2$ 4d$_{xz}$ 4d$_x^2$-$_y^2$, 4s 3p$_y$ 3p$_z$ 3p$_x$ 3d$_{xy}$ 3d$_{yz}$ 3d$_z^2$ 3d$_{xz}$ 3d$_x^2$-$_y^2$, 2s 2p$_y$ 2p$_z$ 2p$_x$, 3s 3p$_y$ 3p$_z$ 3p$_x$, 2s 2p$_y$ 2p$_z$ 2p$_x$. This approach resulted in a charge spilling of less than 4.1% for all simulated pressures.

Supporting Information

Supporting Information is available from the Wiley Online Library or from the author.

Conflict of Interest

The authors declare no conflict of interest.

Author Contributions

Y.W. conceived and designed the project. Y.W., D.Z., and Y.R. performed the X-ray diffraction experiments. Y.W., S.M., W.Z., P.K., M.K., and A.Y. conducted the Raman measurements. V.B. and S.K. carried out the theoretical computation. Y.W. wrote the manuscript with the input of the theoretical computation from V.T.B. and S.V.K.

Data Availability Statement

The data that support the findings of this study are available in the supplementary material of this article.

[1] C. T. Chen, G. L. Wang, X. Y. Wang, Z. Y. Xu, *Appl. Phys. B* **2009**, *97*, 9.

[2] H. Yu, W. Zhang, J. Young, J. M. Rondinelli, P. S. Halasyamani, *Adv. Mater.* **2015**, *27*, 7380.

[3] H. Yu, J. Cantwell, H. Wu, W. Zhang, K. R. Poeppelmeier, P. S. Halasyamani, *Cryst. Growth Des.* **2016**, *16*, 3976.

[4] a) Y. Chen, X. Zhu, S. Ma, H. Yu, H. Wu, Z. Hu, Y. Wu, *Opt. Mater. Express* **2023**, *13*, 3164; b) Y. Chen, J. Wu, J. Wang, S. Ma, H. Yu, *Optical Materials* **2024**, *147*, 114565.

[5] a) V. G. Dmitriev, G. G. Gurzadyan, D. N. Nikogosyan, in *Handbook of Nonlinear Optical Crystals*, (Eds: V. G. Dmitriev, G. G. Gurzadyan, D. N. Nikogosyan), Springer, Berlin, Heidelberg **1999**; b) G. J. Exarhos, A. H. Guenther, D. Ristau, K. L. Lewis, M. J. Soileau, C. J. Stolz, presented at in *Conference: 5991*, SPIE- The International Society for Optical Engeneering, SPIE, Bellingham, WA, USA **2005**.

[6] a) Y. Wang, J. E. Panzik, B. Kiefer, K. K. M. Lee, *Sci. Rep.* **2012**, *2*, 520; b) Y. Wang, K. K. M. Lee, *J. Superhard Mater.* **2012**, *34*, 360.

[7] B. H. Toby, R. B. Von Dreele, *J. Appl. Crystallogr.* **2013**, *46*, 544.

[8] a) F. Birch, *Phys. Rev.* **1947**, *71*, 809; b) F. D. Murnaghan, *Proc. Natl. Acad. Sci. USA* **1944**, *30*, 244.

[9] J. Gonzalez-Platas, M. Alvaro, F. Nestola, R. Angel, *J. Appl. Crystallogr.* **2016**, *49*, 1377.

[10] a) A. L. Goodwin, D. A. Keen, M. G. Tucker, *Proc. Natl. Acad. Sci. USA* **2008**, *105*, 18708; b) A. D. Fortes, E. Suard, K. S. Knight, *Science* **2011**, *331*, 742; c) A. B. Cairns, A. L. Goodwin, *Phys. Chem. Chem. Phys.* **2015**, *17*, 20449.

[11] M. I. Aroyo, J. M. Perez-Mato, C. Capillas, E. Kroumova, S. Ivantchev, G. Madariaga, A. Kirov, H. Wondratschek, *Zeitschrift für Kristallographie – Crystalline Materials* **2006**, *221*, 15.

[12] P. J. Brown, A. G. Fox, E. N. Maslen, M. A. O'Keefe, B. T. M. Willis, *International Tables for Crystallography*, Wiley-VCH, Weinheim, Germany **2006**, pp. 554–595.

[13] K. Momma, F. V. Izumi, *J. Appl. Crystallogr.* **2011**, *44*, 1272.

[14] R. Dronskowski, P. E. Bloechl, *J. Phys. Chem.* **1993**, *97*, 8617.

[15] J. X. H. K. Mao, P. M. Bell, *J. Geophys. Res.-Solid Earth* **1986**, *91*, 4673.

[16] a) D. Errandonea, R. Boehler, S. Japel, M. Mezouar, L. R. Benedetti, *Phys. Rev. B* **2006**, *73*, 092106; b) S. Klotz, J. C. Chervin, P. Munsch, G. L. Marchand, *J. Phys. D-Appl. Phys.* **2009**, *42*, 075413.

[17] M. Rivers, V. B. Prakapenka, A. Kubo, C. Pullins, C. M. Holl, S. D. Jacobsen, *High Pressure Res* **2008**, *28*, 273.

[18] C. Prescher, V. B. Prakapenka, *High Pressure Res* **2015**, *35*, 223.

[19] a) G. Kresse, J. Furthmüller, *Comput. Mater. Sci.* **1996**, *6*, 15; b) G. Kresse, J. Furthmuller, *Phys. Rev. B* **1996**, *54*, 11169; c) G. Kresse, J. Hafner, *Phys. Rev. B* **1993**, *47*, 558.

[20] a) P. E. Blöchl, *Phys. Rev. B* **1994**, *50*, 17953; b) G. Kresse, D. Joubert, *Phys. Rev. B* **1999**, *59*, 1758.

[21] J. P. Perdew, A. Ruzsinszky, G. I. Csonka, O. A. Vydrov, G. E. Scuseria, L. A. Constantin, X. Zhou, K. Burke, *Phys. Rev. Lett.* **2008**, *100*, 136406.

[22] a) S. V. Khare, T. L. Einstein, *Surf. Sci.* **1994**, *314*, L857; b) S. Kodambaka, S. V. Khare, W. Święch, K. Ohmori, I. Petrov, J. E. Greene, *Nature* **2004**, *429*, 49.

[23] a) P. E. Blöchl, O. Jepsen, O. K. Andersen, *Phys. Rev. B* **1994**, *49*, 16223; b) P. P. Gunaicha, S. Gangam, J. L. Roehl, S. V. Khare, *Sol. Energy* **2014**, *102*, 276.

[24] A. Togo, I. Tanaka, *Scr. Mater.* **2015**, *108*, 1.

[25] a) V. L. Deringer, A. L. Tchougréeff, R. Dronskowski, *J. Phys. Chem. A* **2011**, *115*, 5461; b) S. Maintz, M. Esser, R. Dronskowski, *Acta Phys. Pol. B* **2016**, *47*, 1165; c) R. Nelson, C. Ertural, J. George, V. L. Deringer, G. Hautier, R. Dronskowski, *J. Comput. Chem.* **2020**, *41*, 1931; d) S. Maintz, V. L. Deringer, A. L. Tchougréeff, R. Dronskowski, *J. Comput. Chem.* **2013**, *34*, 2557; e) S. Maintz, V. L. Deringer, A. L. Tchougréeff, R. Dronskowski, *J. Comput. Chem.* **2016**, *37*, 1030.